
Article:
Zhang, Yilong, Feng, Zhengshuyi, Huang, Zhihong et al. (2024) Characterizing Viscoelasticity of Corneal Stromal Models Using Non-Contact Air-Pulse Optical Coherence Elastography (OCE) and Validating Using Ramp–Hold Relaxation Testing. Photonics. 24. ISSN: 2304-6732

https://doi.org/10.3390/photonics12010024

---

photonics

MDPI

Article

Characterizing Viscoelasticity of Corneal Stromal Models Using Non-Contact Air-Pulse Optical Coherence Elastography (OCE) and Validating Using Ramp–Hold Relaxation Testing

Yilong Zhang [1], Zhengshuyi Feng [2], Zhihong Huang [2] and Chunhui Li [1,*]

[1] Centre of Medical Engineering and Technology, University of Dundee, Dundee DD1 4HN, UK
[2] School of Physics and Engineering Technology, University of York, York YO10 5DD, UK
* Correspondence: c.li@dundee.ac.uk

Abstract: Corneal biomechanical properties are closely related to the cornea's physiological and pathological conditions, primarily determined by the stromal layer. However, little is known about the influence of corneal cell interaction on the viscoelasticity of the stromal extracellular matrix (ECM). In this study, collagen-based hydrogels incorporated with keratocytes were reconstructed as corneal stromal models. Air-pulse optical coherence elastography (OCE) was used to characterize the viscoelastic properties of the corneal models. Plate compression, ramp–hold relaxation testing was performed on the initial corneal models. The findings demonstrated that the elastic modulus increased 5.27, 2.65 and 1.42 kPa, and viscosity increased 0.22, 0.06 and 0.09 Pa·s in the stromal models with initial collagen concentrations of 3, 5, and 7 mg/mL over 7 days. The elastic modulus and viscosity exhibited high correlation coefficients between air-pulse OCE and ramp–hold relaxation testing, with 92.25% and 98.67%, respectively. This study enhances the understanding of the influence of cell–matrix interactions on the corneal viscoelastic properties and validates air-pulse OCE as an accurate method for the mechanical characterization of tissue-engineered materials.

Keywords: corneal stromal model; viscoelasticity; collagen-based hydrogels; air-pulse optical coherence elastography; surface acoustic wave; ramp–hold relaxation testing

Received: 15 November 2024
Revised: 14 December 2024
Accepted: 26 December 2024
Published: 30 December 2024

Citation: Zhang, Y.; Feng, Z.; Huang, Z.; Li, C. Characterizing Viscoelasticity of Corneal Stromal Models Using Non-Contact Air-Pulse Optical Coherence Elastography (OCE) and Validating Using Ramp–Hold Relaxation Testing. *Photonics* **2025**, *12*, 24. https://doi.org/10.3390/photonics12010024

1. Introduction

The cornea plays a crucial role in vision, providing about two-thirds of the eye's optical power. It also acts as a structural barrier to protect the eye from infections [1]. Recently, corneal biomechanics have gained attention in ophthalmology as these are a determinant of corneal shape. Meanwhile, corneal biomechanical properties are able to aid in the diagnosis and management of corneal diseases as these are closely related to physiopathological conditions [2]. For instance, in keratoconus, the extracellular matrix (ECM) of the cornea is disproportionally degraded, resulting in biomechanical weakening and corneal bulging into a conical shape [3]. This change leads to a reduced elastic modulus and altered viscoelasticity, which may result in corneal ectasia.

The corneal stroma makes up around 85% of the overall cornea's thickness and is primarily responsible for its biomechanical properties [1]. Tissue-engineering techniques have been used to replicate the three-dimensional (3D) architecture of the cornea [4,5]. Hydrogels are a typical scaffold material with biocompatibility and tunable biomechanical properties. Collagen-based hydrogels incorporated with keratocytes are suitable for recon-

structing the human corneal stroma as their compositions, and viscoelastic properties [6] are similar to the natural stroma.

Conventional mechanical testing, such as compression or tensile testing, is a common and gold-standard approach for assessing the mechanical properties of biological [7,8] or engineered tissues [9,10]. In these tests, the sample's response to induced changes is typically monitored by a load cell, while displacement is measured through a mechanical actuator [11]. The elastic modulus can be calculated from the resulting stress–strain curve. Viscoelasticity is assessed by measuring the time-dependent stress–strain response to a constant strain or stress in the uniaxial creep or stress relaxation testing [11]. However, conventional mechanical testing methodologies usually require direct interaction with the sample, making them inherently non-sterile and destructive. Furthermore, these methods provide only bulk mechanical properties of the sample, whereas most native tissues are heterogeneous in nature [12].

Non-contact tonometers such as the ocular response analyzer (ORA) [13] and Corvis ST [14] are utilized in clinical practice to characterize corneal biomechanical properties. These instruments employ an air pulse to displace the central cornea while an infrared beam monitors its bidirectional movement. However, the obtained viscoelastic parameters disagreed in detecting the biomechanical variations in keratoconic cornea before and after cross-linking treatments when compared to pathological or therapeutic results [15,16].

Optical coherence tomography (OCT) is a non-invasive optical imaging modality that provides high-resolution visualization of microstructures in biological soft tissues [17]. Building upon OCT, wave-based optical coherence elastography (OCE) characterizes the biomechanical characteristics of soft tissues by applying external stimuli and analyzing induced elastic waves [18]. The millimeter penetration depth in OCE constrains the motion measurements to regions closer to the tissue boundaries, where surface acoustic waves (SAWs) are the dominant perturbations [19]. Air-pulse OCE generates SAWs for elastography by using a micro-air pulse to deliver a localized impulse stimulus towards the tissue surface. This technique has been used to assess corneal elasticity [20,21] and viscoelasticity [22,23], and to characterize the mechanical properties of tissue-engineered models [24].

In this study, a focused air-pulse OCE system was used to monitor changes in the dimensions and viscoelastic properties of the corneal stromal models made by hydrogels with initial collagen concentrations of 3 mg/mL, 5 mg/mL and 7 mg/mL over a culture period of seven days. An independent compression, ramp–hold relaxation test was conducted to validate the initial viscoelastic parameters of the corneal models. This study enhances the understanding of the influence of cell–matrix interactions on the viscoelasticity of corneal stroma.

2. Materials and Methods

2.1. Corneal Stromal Models

Human keratocytes (P10872, Innoprot, Bizkaia, Spain) were used at passage 3, expanded from a cryo-preserved stock. Keratocytes were cultured in a T25 cell culture flask with the culture media. Culture media consisted of low-glucose Dulbecco's modified Eagle's medium (DMEM, 1.0 g/L glucose, Lonza, Basel, Switzerland) supplemented with 10% fetal bovine serum (FBS, Thermo Fisher Scientific Inc., Waltham, MA, USA) and 1% antibiotic and antimitotic solution (PEN-STREP 5000 U penicillin/m, 5000 U streptomycin/mL, Lonza, Basel, Switzerland). Keratocytes were incubated in 5% carbon dioxide (CO_2) at 37 °C and then trypsinized with 1× EDTA at 80% confluence. The cell number was counted by a hemacytometer.

The stroma-mimicking collagen hydrogels were fabricated in a sterile flow hood. Rat-tail collagen type I (9.1 mg/mL, Corning, NY, USA) was used as the collagen biopolymer in the hydrogel scaffold. In addition, 10 × standard DMEM was added to the collagen solution to neutralize acetic acid. Collagen concentrations of 3 mg/mL, 5 mg/mL and 7 mg/mL were diluted from the original collagen type I solution by the culture media. Keratocytes with a density of 5×10^5 cells/mL were suspended in the collagen solution. Hydrogels without cells were fabricated as a control.

Dome-shaped and cylindrical hydrogels were manufactured (Figure 1). A sterile cellulose filter paper ring with outer and inner diameters of 8 mm and 5 mm, respectively, was prepared as the base for dome-shaped hydrogels to confine its shape to the cornea. The ring was placed on a hydrophobic polytetrafluoroethylene (PTFE) board piece, and the collagen solution with a volume of 80 µL was dropped onto the ring (Figure 1 (blue arrows)). No-cell cylindrical hydrogels were formed by dropping 502 µL hydrogel solution into a customized nylon mold with a height of 10 mm and a diameter of 8 mm (Figure 1 (green arrows)). The hydrogels were gelated on the PTFE board for 2 h in an incubator. The bottom surface of the hydrogel, in direct contact with the PTFE board, remained flat. Subsequently, the formed hydrogel was transferred into a cell culture plate with supplemented culture media.

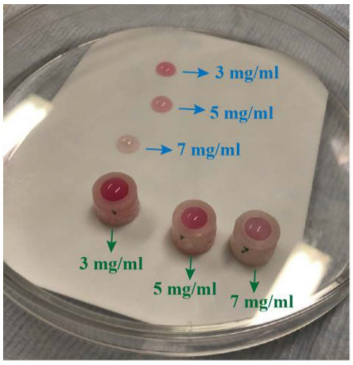

Figure 1. Dome-shaped (blue arrows) and cylindrical shape (green arrows) collagen hydrogels with initial collagen concentrations of 3 mg/mL, 5 mg/mL and 7 mg/mL.

2.2. Cell Image Acquisition

A light microscope (CKX41, Olympus, Tokyo, Japan) was employed to observe the confluence and morphology of keratocytes in stromal models every 24 h. The microscopic image was recorded with a CMEX camera (DC. 5000, Euromex Microscopen, Arnhem, The Netherlands) and analyzed with Image focus v3.0.

2.3. Air-Pulse OCE Setup for Surface Acoustic Wave (SAW) Imaging

In this study, a non-contact air-pulse OCE system was developed to induce and track the impulse SAW propagating within stromal models. The viscoelastic properties were continuously monitored by analyzing the dispersion of SAW phase velocity. The air-pulse OCE system (Figure 2) consisted of an air-pulse generation system and a spectral-domain OCT (SD-OCT) system.

A broadband superluminescent diode (SLD) laser (LS2000B, Thorlabs Inc., Newton, NJ, USA) with a wavelength of 1310 ± 110 nm was employed as the laser source for the SD-OCT system. The interference spectrum was captured by a high-speed InGaAs linear array camera with a maximum sampling frequency of 91,912 Hz. The axial and lateral resolution of this system was approximately 6.9 µm and 23.5 µm in air.

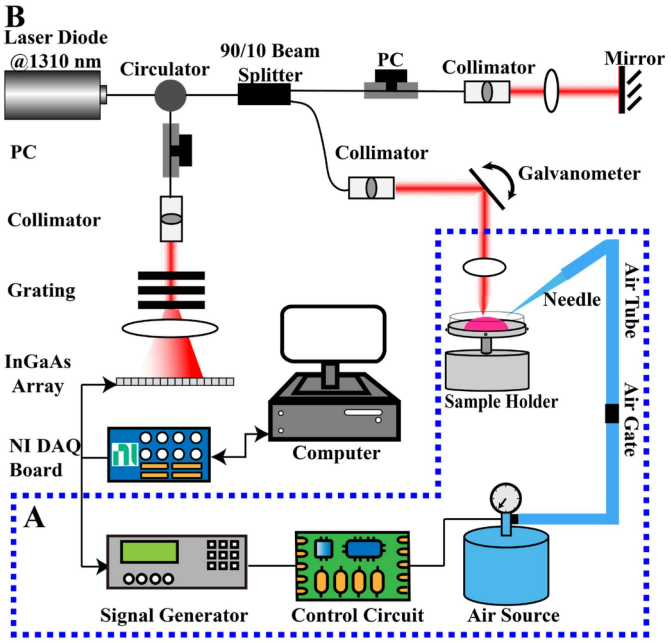

Figure 2. Schematic of an air-pulse OCE system for the SAW imaging in stromal model. (**A**) an air-pulse generation part, and (**B**): a PhS-OCT system PC: polarization controller; DAQ: data acquisition; NI: national instrument.

In the air-pulse generation system, a pneumatic solenoid valve (V114-6 M-M5, SMC Corporation, Tokyo, Japan) and a customized circuit controlled the duration of an air stream. The air-pulse generation system was synchronized with the SD-OCT system through the output signal. The output air pressure was controlled by a pressure control valve on an air compressor (Tayside Compressor Services, Dundee, UK). An externally triggered function generator (33220A, Keysight Technologies Inc., Santa Rosa, CA, USA) was utilized to drive the air-pulse system by a square wave with a frequency of 40 Hz, an amplitude of 5.0 volts peak-to-peak (V_{pp}), an offset of +2.5 volts direct current (V_{dc}) and a duty cycle of 60%. The air pulse delivery was through a needle (KDS3012P, Weller, Besigheim, Germany) with an inner diameter of 0.15 mm. The needle position was accurately altered with a 3D translation stage for the focused air-pulse excitation. The excitation angle of the air stream relative to the surface normal was controlled at 45°. The air pressure was set to be 1 bar, which produced a SAW pulse with a maximum amplitude of 250 nm on the stromal model surface.

The central cross-sectional plane of the stromal model was chosen for SAW imaging. The propagation of the impulse SAW was acquired using an M-B scanning mode. In this mode, 512 A-scans with a sampling frequency of 20,730 Hz were acquired at the same position, generating an M-scan first. Next, 512 successive M-scans with a frame rate of 30 Hz and lateral spacing of 17 μm were acquired laterally. One complete M-B scan required 18.9 s. As a result, each stromal model was acquired with an average of 75.6 s. The size of the experimental imaging plane was ~2.11 mm in depth × ~9 mm in lateral distance. The wave propagation data were acquired and stored by a LabView (V2016, National Instruments, Austin, TX, USA) program.

2.4. Central Thickness Measurement

The central thickness of the stromal models was extracted from the central cross-sectional OCT structural image. The imaging depth was 2.8 mm in air, corresponding to 2.11 mm in the stromal model (assuming the refractive index as 1.333 [25]). The size of

each pixel was calculated to be 4.12 μm based on 512 pixels acquired in depth. The central thickness of the stromal model can be obtained as follows:

$$CT_h = P_h \times L_p \tag{1}$$

where CT_h denotes the central thickness of the stromal model, P_h represents the pixel number from peak to bottom, and L_p is the length of each pixel.

2.5. Viscoelastic Characterization of Stromal Models Based on SAW Phase Velocity

In a homogenous, intrinsically viscoelastic material, dispersion behavior occurs during the SAW propagation. SAW propagates with various phase velocities at different frequency components. Therefore, phase velocities at each frequency component are able to depict the propagation of SAW in the viscoelastic material. Under this background, the material viscoelasticity can be inferred by the phase velocity dispersion of a SAW pulse [26].

The post-processing steps to extract the SAW phase velocity and estimate the viscoelastic parameters of the stromal models are described in our previous publication [24]. First, an area of 1.6 mm in lateral distance × 0.47 in depth (Figure 3A, yellow dashed rectangle) was selected from the central cross-sectional structural image (Figure 3A). Most of the SAW energy remained on the free surface of the sample [27]. The upper boundary of the stromal model was detected. The lower boundary was determined as 20 axial pixels (~94 μm in depth, Figure 3B, blue line) below the upper boundary. The phase difference between the boundaries was averaged for signal-to-noise ratio (SNR) enhancement in SAW. The axial displacement ($\Delta z(z,t)$) was estimated from the phase difference as follows [28]:

$$\Delta z(z,t) = \frac{\lambda_c \Delta \Phi z(z,t)}{4\pi n} \tag{2}$$

where $\Delta \Phi z(z,t)$ represents the phase difference between two consecutive A-lines, λ is the central wavelength of laser source, and n is the refractive index of the medium. Thus, a spatial–temporal displacement map was obtained (Figure 3C). Next, a 2D FFT was applied to the spatial–temporal displacement map to obtain a wavenumber–frequency map (Figure 3D). A phase velocity intensity map was generated by estimating the phase velocities of the SAW at each frequency component as follows [29]:

$$C_p = \frac{\omega}{k} \tag{3}$$

where C_p denotes the phase velocity, ω represents the angular frequency and k is the wave number. The maximum intensity of the phase velocity at each frequency was used to derive the phase velocity dispersion curve. The dispersion curve at a frequency range between 600 Hz and 900 Hz was chosen to determine the shear modulus and viscosity. The selected dispersion curve was finally fitted into a Rayleigh wave dispersion model, which can be written as follows [18]:

$$C_R(\omega) = 0.955 \sqrt{\frac{2\left(\mu_1^2 + \omega^2 \mu_2^2\right)}{\rho\left(\mu_1 + \sqrt{\mu_1^2 + \omega^2 \mu_2^2}\right)}} \tag{4}$$

where C_R is the SAW phase velocity, μ_1 and μ_2 denote the shear modulus and shear viscosity, and ω denotes the angular frequency. The density ρ was assumed to be as same as the water at 37 °C (993 kg/m^3) [30].

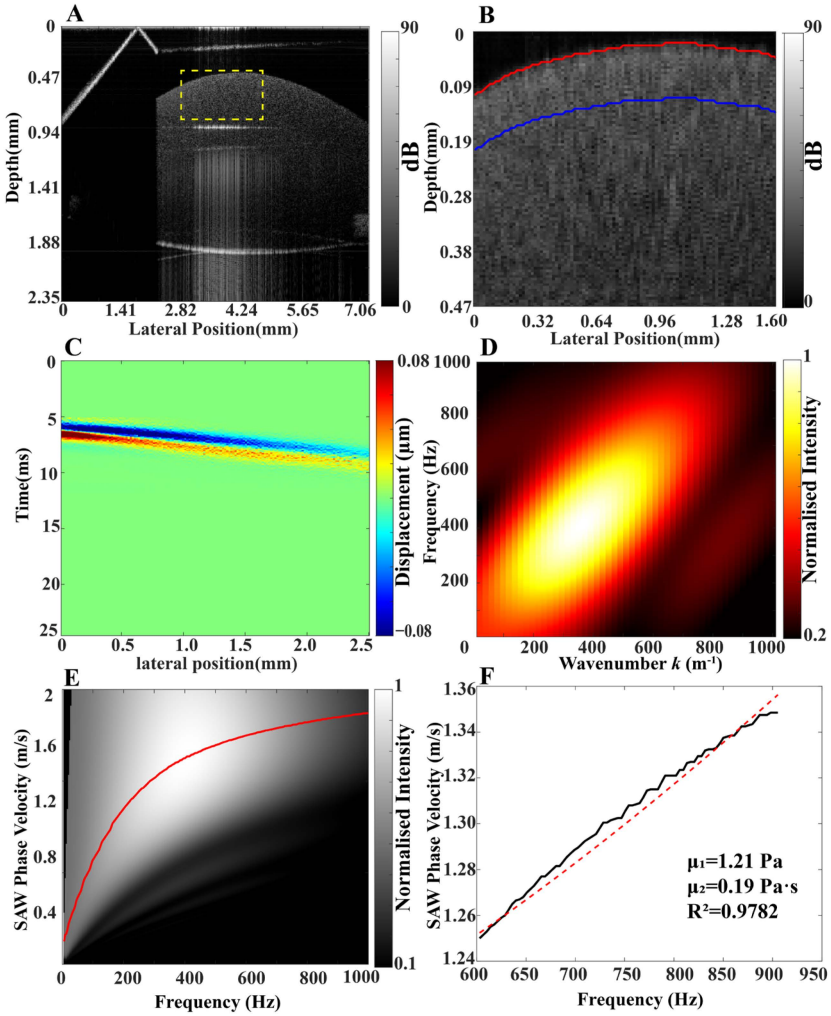

Figure 3. Signal-processing steps of a 5 mg/mL cell-seeded stromal model on day 1. (**A**) The central cross-sectional structural image. (**B**) The structural image of the yellow dashed rectangle. The red and blue solid lines illustrate the boundaries of the analyzed region. (**C**) The spatial–temporal displacement map of the impulse SAW. (**D**) The wavenumber–frequency domain map of the impulse SAW. (**E**) The phase velocity dispersion curve (red solid line) overlaps the grayscale intensity map. (**F**) fitting the dispersion curve (black solid line) into the Rayleigh wave dispersion model. Red solid line: fitting curve; μ_1: shear modulus; μ_2: shear viscosity; R^2: coefficient of determination.

The relationship between elastic modulus (Young's modulus, E) and shear modulus (μ_1) can be written as follows:

$$E = 2\mu_1(1 + v) \quad (5)$$

where E is the elastic modulus of the material, and the Poisson's ratio v of the stromal models was assumed as 0.5 [31] as the stromal models were immersed in the culture media. Assuming isotropy, the shear modulus (μ_1) is proportional to the elastic modulus (E), according to the expression $E = 3\ \mu_1$.

2.6. Plate Compression, Ramp–Hold Stress Relaxation Test

Step compressions are used in most load relaxation studies for the analytical simplicity of deriving a step–hold relaxation response solution. However, applying a near-step strain often results in oscillatory transients on the material's application, causing a significant loss of accuracy in model fitting [32]. The ramp–hold relaxation response significantly improves model-fitting accuracy by preventing oscillated artefacts in measurements [33]. In this study, a ramp–hold plate compression relaxation experiment (Figure 4) was performed

on the cylindrical stromal model with different collagen concentrations to validate the accuracy of viscoelastic properties measured by the air-pulse OCE. The test was carried out by a Tinius Olsen H5KS material test machine (Tinius Olsen Ltd., Salfords, UK) at room temperature.

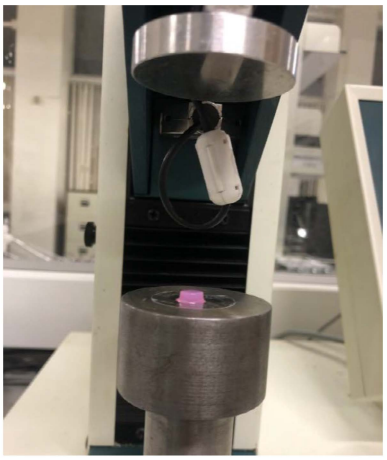

Figure 4. Experimental apparatus for the plate compression, ramp–hold stress relaxation test. Cylindrical stromal model placed on the testing plate of a Tinius Olsen H5KS material test machine.

In this experiment, cylindrical no-cell stromal models were examined. The compression speed was set to be 2 mm/min, and the ramp time was set to be 45 s. When the plate compressor reached the set maximum displacement (15% strain, 1.5 mm), the plate was held for 300 s to measure stress relaxation. The force relaxation data during the test were obtained. Then, the relaxation data were fitted into a Kelvin–Voigt fractional derivative (KVFD) model [32] to estimate the viscoelastic parameters. The KVFD model is given by:

$$\sigma_r(t) = \begin{cases} \frac{\varepsilon_0 E_0 t}{T_r}\left[1 + \frac{(t/\tau)^{-\alpha}}{\Gamma(2-a)}\right], 0 \le t \le T_r \\ \frac{\varepsilon_0 E_0 t}{T_r}\left[T_r - (t-T_r)\frac{((t/T_r)/\tau)^{-\alpha}}{\Gamma(2-a)} + t\frac{(t/\tau)^{-\alpha}}{\Gamma(2-\alpha)}\right], t > T_r \end{cases} \quad (6)$$

where σ_r is the stress relaxation response, T_r denotes the duration of the ramp, E_0 represents the elastic modulus of the sample, τ is the relaxation time constant and α is the derivative order. Thus, the viscoelastic parameters of the stromal model, including the elastic modulus (E_0) and the normalized time-dependent viscosity $\eta = E_0 \cdot \tau^{\alpha}$, were estimated.

The correlation between viscoelastic parameters calculated by air-pulse OCE and the ramp–hold relaxation test was assessed using pairwise correlation in MATLAB (R2020b, The MathWorks Inc., Natick, MA, USA).

3. Results

3.1. Morphology of Keratocytes in Stromal Model Cultures

Figure 5 shows the morphology and confluency of keratocytes in the stromal models with initial collagen concentrations of 3, 5, and 7 mg/mL on day 3 and day 7. The results showed that stromal models with a lower initial collagen concentration exhibited a more significant increase in cell proliferation than models with a higher initial collagen concentration. The stromal model with an initial collagen concentration of 3 mg/mL had the fastest proliferation rate for 7 days. The 5 mg/mL stromal model showed a noticeable increase in cell population from day 3 to day 7. In contrast, the 7 mg/mL stromal model had a slow rate of cell proliferation and less change in cell population between day 3 and day 7.

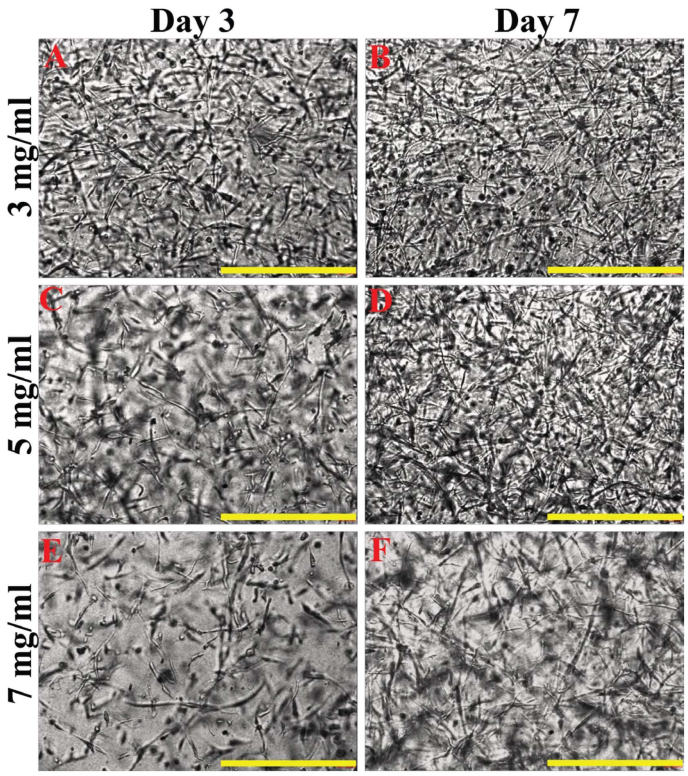

Figure 5. Light microscopic images of keratocytes in cell-seeded stromal models with initial collagen concentrations of 3 mg/mL (**A**,**B**), 5 mg/mL (**C**,**D**) and 7 mg/mL (**E**,**F**) on day 3 and day 7. Scale bar = 500 μm.

3.2. Central Thickness of Stromal Models

The central thickness of stromal models was monitored for 7 days (Figure 6). The central thickness of the no-cell stromal models with initial collagen concentrations of 3, 5, and 7 mg/mL was steady at approximately 1.44 mm, 1.74 mm, and 1.69 mm over the culture period. The center thickness of the cell-seeded stromal models with a lower initial collagen concentration decreased faster than that of those with a greater initial collagen concentration. Quantitatively, the central thickness of the cell-seeded stromal model with an initial collagen concentration of 3 mg/mL decreased by 34.7%, from 1.18 ± 0.18 mm on day 1 to 0.77 ± 0.03 mm on day 7 (Figure 6A). The central thickness of the 5 mg/mL cell-seeded stromal model experienced a significant decrease from day 3 at 1.48 ± 0.07 mm to day 7 at 1.04 ± 0.07 mm, with a contraction of 30% (Figure 6B). The central thickness of the cell-seeded stromal model with an initial collagen concentration of 7 mg/mL exhibited less change throughout the time, decreasing from 1.71 ± 0.09 mm to 1.68 ± 0.06 mm, equal to a 2% contraction of the initial central thickness (Figure 6C).

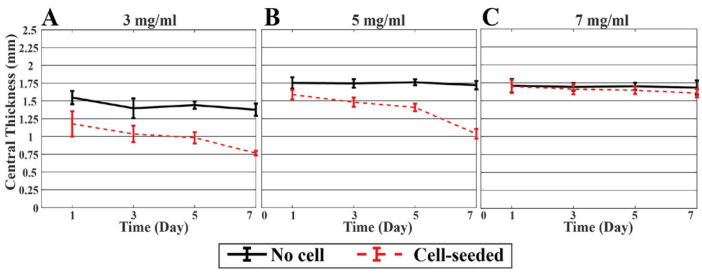

Figure 6. Central thickness of cell-seeded (red dashed line) and no-cell (black solid line) stromal models with initial collagen concentrations of 3 mg/mL (**A**), 5 mg/mL (**B**) and 7 mg/mL (**C**) in 7 days.

3.3. Viscoelastic Properties of Stromal Models from Air-Pulse OCE

The elastic modulus and viscosity of the stromal models with initial collagen concentrations of 3 mg/mL, 5 mg/mL, and 7 mg/mL were monitored with the air-pulse OCE system over 7 days (Figure 7). The elastic modulus of the cell-seeded stromal models with an initial collagen concentration of 3 mg/mL significantly increased from 2.07 ± 0.07 kPa on day 1 to 7.34 ± 0.19 kPa on day 7. Meanwhile, the viscosity increased from 0.09 ± 0.02 Pa·s to 0.31 ± 0.02 Pa·s. The elastic modulus and the viscosity of the 5 mg/mL model had a considerable increase between day 3 (4.36 ± 0.64 kPa; 0.27 ± 0.03 Pa·s) and day 7 (6.43 ± 1.58 kPa; 0.33 ± 0.17 Pa·s). The viscoelastic parameters of the 7 mg/mL model increased by 1.42 kPa and 0.09 Pa·s in 7 days. In comparison, the no-cell models with the initial concentration of 3 mg/mL, 5 mg/mL and 7 mg/mL kept steady at the elastic modulus of ~2.10 kPa, ~2.80 kPa, and ~4.80 kPa, and the viscosity of ~0.05 Pa·s, ~0.09 Pa·s, ~0.25 Pa·s over 7 days. The results showed that the cell-seeded stromal models with lower initial collagen concentrations had lower initial viscoelasticity and less resistance to viscoelastic changes.

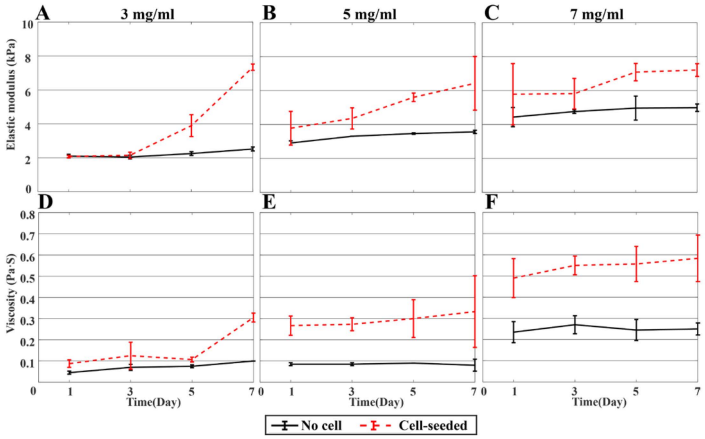

Figure 7. Elastic modulus (**A**–**C**) and viscosity (**D**–**F**) of no-cell (black solid line) and cell-seeded (red dashed line) stromal models with initial collagen concentrations of 3 mg/mL (**A**,**D**), 5 mg/mL (**B**,**E**) and 7 mg/mL (**C**,**F**).

3.4. Viscoelastic Properties of Stromal Models from Plate Compression, Ramp–Hold Relaxation Test

The original ramp–hold relaxation and KVFD fitting curves for the cylindrical no-cell stromal models with three collagen concentrations on day 1 are displayed in Figure 8. The curves contained the compression part (before 45 s) and the force relaxation part (from 45 s to 300 s). A greater slope of the compression region for the stromal models with higher initial collagen concentrations was performed, indicating a higher elastic modulus. Also, a greater rate of stress loss was found during the relaxation part, representing a higher viscosity.

The viscoelastic parameters of the 3 mg/mL, 5 mg/mL, and 7 mg/mL stromal models obtained from fitting the stress relaxation curves into the KVFD model are summarized in Table 1. The elastic modulus increased from 1.01 ± 0.12 kPa for the 3 mg/mL stromal model to 1.46 ± 0.14 kPa for the 7 mg/mL model. The normalized time-dependent viscosity also increased with collagen concentrations of the models (from 3 mg/mL: 27.71 ± 1.03 Pa·s to 7 mg/mL: 33.55 ± 1.03 Pa·s). These viscoelastic parameters validated this from air-pulse OCE through a linear dependence analysis. Both elastic modulus and viscosity exhibited high correlation coefficients, with 92.25% and 98.67%, respectively. Therefore, air-pulse OCE was reliable in characterizing the viscoelastic properties of the stromal models with initial collagen concentrations of 3 mg/mL, 5 mg/mL and 7 mg/mL.

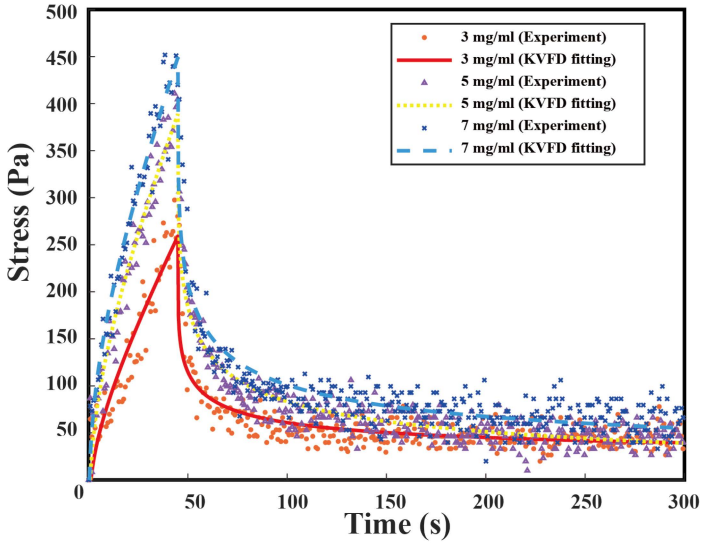

Figure 8. Plate compression, ramp–hold relaxation curves for no-cell stromal models with initial collagen concentrations of 3 mg/mL, 5 mg/mL and 7 mg/mL with corresponding KVFD model fitting.

Table 1. Estimated elastic modulus, normalized time-dependent viscosity from KVFD model and correlation coefficient with air-pulse OCE results.

Concentrations	Elastic Modulus	Normalized Viscosity
3 mg/mL	1.01 ± 0.12 kPa	27.71 ± 1.03 Pa·s
5 mg/mL	1.26 ± 0.11 kPa	28.90 ± 1.05 Pa·s
7 mg/mL	1.46 ± 0.14 kPa	33.55 ± 1.03 Pa·s
Coefficient	92.25%	98.67%

4. Discussion

This study investigated the effect of interactions between stromal cells and ECM on the viscoelastic properties of corneal-stroma-mimicking collagen hydrogels in a continuous culture period. A phase-stabilized air-pulse OCE system was developed to evaluate the dimension and viscoelasticity of the stromal models with three different collagen concentrations over 7 days. The elastic modulus and viscosity were calculated based on the impulse SAW phase velocity and then fitted into a Rayleigh wave dispersion equation. In plate compression, ramp–hold relaxation testing, the force relaxation curve was measured and fitted into a KVFD model for obtaining the viscoelastic parameters of stromal models.

The main benefits of this study are as follows: (1) a completely non-contact air-pulse system to prevent stromal models from contamination; (2) a small displacement induced by the air stream to prevent deformation of stromal models during the culture period; (3) consecutive monitoring of the viscoelastic properties of stromal models with initial collagen concentrations of 3 mg/mL, 5 mg/mL and 7 mg/mL; (4) the viscoelastic results from the SAW dispersion model validated by a stress relaxation test.

Strain OCE provides high-resolution biomechanical distribution maps of samples [34] by using direct compression [35] or a laser-induced method [36] to acquire non-linear stress–strain curves or stress relaxation data, enabling a potential estimation of viscoelastic properties. Additionally, commonly used wave-based OCE techniques, such as focused ultrasound [27] or piezoelectric transducer-induced [37] OCE, facilitate straightforward viscoelastic measurements. In contrast, air-pulse OCE can perform continuous biomechanical measurements of samples while avoiding contamination due to its non-contact excitation method.

In this study, the central thickness (Figure 6) revealed that the stromal models with greater collagen concentrations had a slower rate of contraction than those with lower concentrations over 7 days. It was evident that the stromal models with lower initial collagen concentrations had less mechanical resistance to the contraction of the ECM. Cell–matrix interactions played a major role in the dimension and viscoelasticity changes. Keratocytes integrated themselves, adhered to the collagen matrix [38], and released ECM products [39] within the stromal models. Consequently, the viscoelastic properties of the surrounding ECM were changed. In turn, the altered ECM property could affect cellular behaviors [40]. Our results showed that the increased cell density led to a higher elastic modulus and viscosity of the stromal models.

The elastic modulus of stromal models with initial collagen concentrations of 3, 5, and 7 mg/mL estimated by the air-pulse OCE exhibited a similar increasing trend to that observed in a previous study [41], which monitored hydrogels with 2.5, 3.5 and 4.5 mg/mL by a spherical indentation technique over 25 days. Fewer changes in the elastic modulus and thickness could also be found in the hydrogels with a higher initial collagen concentration. By contrast, we examined a wider range of initial collagen concentrations, allowing us to draw broader conclusions. Moreover, the hydrogels' viscosity was considered in this study. Regarding the viscosity of hydrogels, the outcomes from Zvietcovich et al. [42] demonstrated that ultrasound-induced OCE was capable of characterizing viscoelasticity by inducing shear waves inside the hydrogels with different collagen concentrations of 2, 5, 6.7 and 10.6 mg/mL. Their findings indicated that the relative viscosity values of the hydrogels with increasing collagen concentrations were approximately equivalent to ours. However, their stimulation technique would contaminate or damage the sample, making it unsuitable for continuous characterization. Compared to our previous study [24], the initial cell-seeded stromal models in this study had a cell density five times higher. This led to more rapid increases in both elasticity and viscosity of the stromal models, demonstrating a positive correlation between cell density and viscoelastic properties of collagen ECM, particularly at lower collagen concentrations.

To advance our current in vitro corneal model toward in vivo artificial corneas, several potential improvements need to be considered. First, the elastic modulus of our stromal models was of less than 10 kPa, significantly lower compared to the native cornea, which has a shear modulus of 72 ± 14 kPa in healthy subjects [43]. At low collagen concentrations, cross-linking becomes necessary to achieve adequate mechanical stiffness [44]. Next, the development of tissue-engineered corneas has been explored to replicate the cornea's three layers (epithelium, stroma, and endothelium) [45] by combining human cells within a highly controlled 3D environment to study complex physiological and pathophysiological processes. Tegtmeyer et al. [46] and Reichl et al. [47] developed full-thickness artificial corneas using collagen-based gel. Third, collagen lamellae make up approximately 90% of corneal thickness and account for the majority of the cornea's anisotropic structure and mechanical behavior [48]. Pitre Jr et al. [49] introduced and fully characterized a nearly incompressible transversely isotropic (NITI) model to measure two shear moduli, thereby decoupling tensile and shear responses. However, the collagen fibers in our model were more random in orientation and relatively homogenous. Thus, we assume it was isotropic and obtained a single shear modulus. To replicate corneal anisotropy in tissue-engineered models for potential in vivo characterization, several methods have been reported to achieve collagen fiber orientation in hydrogels [50,51]. Fourth, intraocular pressure (IOP) significantly correlates with corneal elasticity [22,52] and viscosity [22]. Currently, the stromal model is supported by a neutral environment, which does not replicate the natural boundary conditions of the eye. One potential future improvement involves incorporating a pressurized liquid backing to simulate IOP, allowing for the introduction of a more

physiologically relevant stress state within the stromal construct. Fifth, although type I collagen is the most abundance in the corneal stroma, other collagen types, including type V and fibril-associated collagens (XII and XIV), also contribute to the cornea's lamellar structure, providing essential mechanical properties [45]. Thus, incorporating additional collagen types could better replicate the native cornea's heterogeneous and hierarchical structure in future work. Lastly, destructive relaxation testing was conducted on the initial stromal models. To provide a more comprehensive validation of the air-pulse OCE results, subsequent studies will incorporate relaxation tests at different time points during the culture period. This will allow for a more detailed assessment of changes in viscoelastic properties and ensure the reliability of OCE measurements over time.

5. Conclusions

In conclusion, this work investigated the influence of interactions between stromal cells and stromal ECM on the viscoelastic properties of corneal stroma models. A non-contact air-pulse OCE technique was used to monitor the dimensional and viscoelastic changes in stromal models over a 7-day culture period. The viscoelastic measurements obtained through air-pulse OCE were validated using independent plate compression, ramp–hold relaxation testing. This study proves the accuracy of air-pulse OCE for mechanical characterization and demonstrates its potential as a reliable tool for evaluating a wide range of tissue-engineered materials.

Author Contributions: Conceptualization, Y.Z. and C.L.; methodology, C.L.; software, Y.Z. and Z.F.; validation Y.Z. and Z.F.; formal analysis, Y.Z. and Z.F.; investigation, Y.Z. and Z.F.; resources, Z.H.; data curation, Y.Z. and Z.F.; writing—original draft preparation, Y.Z.; writing—review and editing, Y.Z., Z.F., C.L. and Z.H.; visualization, Y.Z.; supervision, C.L. and Z.H.; project administration, Z.H. All authors have read and agreed to the published version of the manuscript.

Funding: This research received no external funding.

Institutional Review Board Statement: Not applicable.

Informed Consent Statement: Not applicable.

Data Availability Statement: The data is available upon request by contacting Dr Chunhui Li (c.li@dundee.ac.uk).

Conflicts of Interest: The authors declare no conflicts of interest.

References

1. DelMonte, D.W.; Kim, T. Anatomy and physiology of the cornea. *J. Cataract Refract. Surg.* **2011**, *37*, 588–598. [CrossRef] [PubMed]
2. Kling, S.; Hafezi, F. Corneal biomechanics—A review. *Ophthalmic Physiol. Opt.* **2017**, *37*, 240–252. [CrossRef] [PubMed]
3. Krachmer, J.H.; Feder, R.S.; Belin, M.W. Keratoconus and related noninflammatory corneal thinning disorders. *Surv. Ophthalmol.* **1984**, *28*, 293–322. [CrossRef] [PubMed]
4. Wang, S.; Ghezzi, C.E.; Gomes, R.; Pollard, R.E.; Funderburgh, J.L.; Kaplan, D.L. In vitro 3D corneal tissue model with epithelium, stroma, and innervation. *Biomaterials* **2017**, *112*, 1–9. [CrossRef]
5. Wilson, S.L.; Wimpenny, I.; Ahearne, M.; Rauz, S.; El Haj, A.J.; Yang, Y. Chemical and topographical effects on cell differentiation and matrix elasticity in a corneal stromal layer model. *Adv. Funct. Mater.* **2012**, *22*, 3641–3649. [CrossRef]
6. Kim, A.; Lakshman, N.; Karamichos, D.; Petroll, W.M. Growth factor regulation of corneal keratocyte differentiation and migration in compressed collagen matrices. *Investig. Ophthalmol. Vis. Sci.* **2010**, *51*, 864–875. [CrossRef] [PubMed]
7. Wollensak, G.; Spoerl, E.; Seiler, T. Stress-strain measurements of human and porcine corneas after riboflavin–ultraviolet-A-induced cross-linking. *J. Cataract Refract. Surg.* **2003**, *29*, 1780–1785. [CrossRef] [PubMed]
8. Yazdi, A.A.; Melchor, J.; Torres, J.; Faris, I.; Callejas, A.; Gonzalez-Andrades, M.; Rus, G. Characterization of non-linear mechanical behavior of the cornea. *Sci. Rep.* **2020**, *10*, 11549.
9. Crabb, R.A.; Chau, E.P.; Evans, M.C.; Barocas, V.H.; Hubel, A. Biomechanical and microstructural characteristics of a collagen film-based corneal stroma equivalent. *Tissue Eng.* **2006**, *12*, 1565–1575. [CrossRef]

10. Long, K.; Liu, Y.; Li, W.; Wang, L.; Liu, S.; Wang, Y.; Wang, Z.; Ren, L. Improving the mechanical properties of collagen-based membranes using silk fibroin for corneal tissue engineering. *J. Biomed. Mater. Res. Part A* **2015**, *103*, 1159–1168. [CrossRef] [PubMed]
11. Fung, Y.-C. Chapter 2. The Meaning of the Constitutive Equation. In *Biomechanics: Mechanical Properties of Living Tissues*; Springer Science & Business Media: Berlin/Heidelberg, Germany, 2013.
12. Luo, L.; Okur, K.E.; Bagnaninchi, P.O.; El Haj, A.J. Current challenges in imaging the mechanical properties of tissue engineered grafts. *Front. Biomater. Sci.* **2024**, *3*, 1323763. [CrossRef]
13. Kopito, R.; Gaujoux, T.; Montard, R.; Touzeau, O.; Allouch, C.; Borderie, V.; Laroche, L. Reproducibility of viscoelastic property and intraocular pressure measurements obtained with the Ocular Response Analyzer. *Acta Ophthalmol.* **2011**, *89*, e225–e230. [CrossRef]
14. Bak-Nielsen, S.; Pedersen, I.B.; Ivarsen, A.; Hjortdal, J. Repeatability, reproducibility, and age dependency of dynamic Scheimpflug-based pneumotonometer and its correlation with a dynamic bidirectional pneumotonometry device. *Cornea* **2015**, *34*, 71–77. [CrossRef] [PubMed]
15. Gkika, M.; Labiris, G.; Giarmoukakis, A.; Koutsogianni, A.; Kozobolis, V. Evaluation of corneal hysteresis and corneal resistance factor after corneal cross-linking for keratoconus. *Graefe's Arch. Clin. Exp. Ophthalmol.* **2012**, *250*, 565–573. [CrossRef] [PubMed]
16. Goldich, Y.; Barkana, Y.; Morad, Y.; Hartstein, M.; Avni, I.; Zadok, D. Can we measure corneal biomechanical changes after collagen cross-linking in eyes with keratoconus?—A pilot study. *Cornea* **2009**, *28*, 498–502. [CrossRef] [PubMed]
17. Yaqoob, Z.; Wu, J.; Yang, C. Spectral domain optical coherence tomography: A better OCT imaging strategy. *Biotechniques* **2005**, *39*, S6–S13. [CrossRef] [PubMed]
18. Kirby, M.A.; Pelivanov, I.; Song, S.; Ambrozinski, L.; Yoon, S.J.; Gao, L.; Li, D.; Shen, T.T.; Wang, R.K.; O'Donnell, M. Optical coherence elastography in ophthalmology. *J. Biomed. Opt.* **2017**, *22*, 121720. [CrossRef] [PubMed]
19. Zvietcovich, F.; Larin, K.V. Wave-based optical coherence elastography: The 10-year perspective. *Prog. Biomed. Eng.* **2022**, *4*, 012007. [CrossRef]
20. Wang, S.; Larin, K.V. Noncontact depth-resolved micro-scale optical coherence elastography of the cornea. *Biomed. Opt. Express* **2014**, *5*, 3807–3821. [CrossRef]
21. Singh, M.; Han, Z.; Li, J.; Vantipalli, S.; Aglyamov, S.R.; Twa, M.D.; Larin, K.V. Quantifying the effects of hydration on corneal stiffness with noncontact optical coherence elastography. *J. Cataract Refract. Surg.* **2018**, *44*, 1023–1031. [CrossRef]
22. Han, Z.; Li, J.; Singh, M.; Wu, C.; Liu, C.-h.; Raghunathan, R.; Aglyamov, S.R.; Vantipalli, S.; Twa, M.D.; Larin, K.V. Optical coherence elastography assessment of corneal viscoelasticity with a modified Rayleigh-Lamb wave model. *J. Mech. Behav. Biomed. Mater.* **2017**, *66*, 87–94. [CrossRef] [PubMed]
23. Han, Z.; Aglyamov, S.R.; Li, J.; Singh, M.; Wang, S.; Vantipalli, S.; Wu, C.; Liu, C.-H.; Twa, M.D.; Larin, K.V. Quantitative assessment of corneal viscoelasticity using optical coherence elastography and a modified Rayleigh–Lamb equation. *J. Biomed. Opt.* **2015**, *20*, 020501. [CrossRef] [PubMed]
24. Zhang, Y.; Zhou, K.; Feng, Z.; Feng, K.; Ji, Y.; Li, C.; Huang, Z. Viscoelastic properties' characterization of corneal stromal models using non-contact surface acoustic wave optical coherence elastography (SAW-OCE). *J. Biophotonics* **2022**, *15*, e202100253. [CrossRef]
25. Schiebener, P.; Straub, J.; Levelt Sengers, J.; Gallagher, J. Refractive index of water and steam as function of wavelength, temperature and density. *J. Phys. Chem. Ref. Data* **1990**, *19*, 677–717. [CrossRef]
26. Li, C.; Guan, G.; Cheng, X.; Huang, Z.; Wang, R.K. Quantitative elastography provided by surface acoustic waves measured by phase-sensitive optical coherence tomography. *Opt. Lett.* **2012**, *37*, 722–724. [CrossRef] [PubMed]
27. Zhou, K.; Li, C.; Chen, S.; Nabi, G.; Huang, Z. Feasibility study of using the dispersion of surface acoustic wave impulse for viscoelasticity characterization in tissue mimicking phantoms. *J. Biophotonics* **2019**, *12*, e201800177. [CrossRef] [PubMed]
28. Wang, R.K.; Kirkpatrick, S.; Hinds, M. Phase-sensitive optical coherence elastography for mapping tissue microstrains in real time. *Appl. Phys. Lett.* **2007**, *90*, 164105. [CrossRef]
29. Zhou, K.; Le, N.; Huang, Z.; Li, C. High-intensity-focused ultrasound and phase-sensitive optical coherence tomography for high resolution surface acoustic wave elastography. *J. Biophotonics* **2018**, *11*, e201700051. [CrossRef]
30. Piskounova, S.; Rojas, R.; Bergman, K.; Hilborn, J. The Effect of Mixing on the Mechanical Properties of Hyaluronan-Based Injectable Hydrogels. *Macromol. Mater. Eng.* **2011**, *296*, 944–951. [CrossRef]
31. Ahearne, M.; Yang, Y.; El Haj, A.J.; Then, K.Y.; Liu, K.-K. Characterizing the viscoelastic properties of thin hydrogel-based constructs for tissue engineering applications. *J. R. Soc. Interface* **2005**, *2*, 455–463. [CrossRef]
32. Zhang, H.; Wang, Y.; Insana, M.F. Ramp-hold relaxation solutions for the KVFD model applied to soft viscoelastic media. *Meas. Sci. Technol.* **2016**, *27*, 025702. [CrossRef]
33. Lee, S.; Knauss, W.G. A note on the determination of relaxation and creep data from ramp tests. *Mech. Time-Depend. Mater.* **2000**, *4*, 1–7. [CrossRef]

34. Zaitsev, V.Y.; Matveyev, A.L.; Matveev, L.A.; Sovetsky, A.A.; Hepburn, M.S.; Mowla, A.; Kennedy, B.F. Strain and elasticity imaging in compression optical coherence elastography: The two-decade perspective and recent advances. *J. Biophotonics* **2021**, *14*, e202000257. [CrossRef] [PubMed]
35. Zaitsev, V.Y.; Matveev, L.A.; Matveyev, A.L.; Plekhanov, A.A.; Gubarkova, E.V.; Kiseleva, E.B.; Sovetsky, A.A. Geophysics-Inspired Nonlinear Stress–Strain Law for Biological Tissues and Its Applications in Compression Optical Coherence Elastography. *Materials* **2024**, *17*, 5023. [CrossRef] [PubMed]
36. Alexandrovskaya, Y.M.; Baum, O.I.; Sovetsky, A.A.; Matveyev, A.L.; Matveev, L.A.; Sobol, E.N.; Zaitsev, V.Y. Observation of internal stress relaxation in laser-reshaped cartilaginous implants using OCT-based strain mapping. *Laser Phys. Lett.* **2020**, *17*, 085603. [CrossRef]
37. Jin, Z.; Zhou, Y.; Shen, M.; Wang, Y.; Lu, F.; Zhu, D. Assessment of corneal viscoelasticity using elastic wave optical coherence elastography. *J. Biophotonics* **2020**, *13*, e201960074. [CrossRef] [PubMed]
38. Takakuda, K.; Miyairi, H. Tensile behaviour of fibroblasts cultured in collagen gel. *Biomaterials* **1996**, *17*, 1393–1397. [CrossRef] [PubMed]
39. Saddiq, Z.A.; Barbenel, J.C.; Grant, M.H. The mechanical strength of collagen gels containing glycosaminoglycans and populated with fibroblasts. *J. Biomed. Mater. Res. Part A Off. J. Soc. Biomater. Jpn. Soc. Biomater. Aust. Soc. Biomater. Korean Soc. Biomater.* **2009**, *89*, 697–706. [CrossRef]
40. Cross, V.L.; Zheng, Y.; Choi, N.W.; Verbridge, S.S.; Sutermaster, B.A.; Bonassar, L.J.; Fischbach, C.; Stroock, A.D. Dense type I collagen matrices that support cellular remodeling and microfabrication for studies of tumor angiogenesis and vasculogenesis in vitro. *Biomaterials* **2010**, *31*, 8596–8607. [CrossRef]
41. Ahearne, M.; Wilson, S.L.; Liu, K.-K.; Rauz, S.; El Haj, A.J.; Yang, Y. Influence of cell and collagen concentration on the cell–matrix mechanical relationship in a corneal stroma wound healing model. *Exp. Eye Res.* **2010**, *91*, 584–591. [CrossRef]
42. Zvietcovich, F.; Rolland, J.P.; Grygotis, E.; Wayson, S.; Helguera, M.; Dalecki, D.; Parker, K.J. Viscoelastic characterization of dispersive media by inversion of a general wave propagation model in optical coherence elastography. In Proceedings of the Optical Elastography and Tissue Biomechanics V, San Francisco, CA, USA, 27 January–1 February 2018; pp. 31–41.
43. Ramier, A.; Eltony, A.M.; Chen, Y.; Clouser, F.; Birkenfeld, J.S.; Watts, A.; Yun, S.-H. In vivo measurement of shear modulus of the human cornea using optical coherence elastography. *Sci. Rep.* **2020**, *10*, 17366. [CrossRef] [PubMed]
44. Lee, K.Y.; Mooney, D.J. Hydrogels for tissue engineering. *Chem. Rev.* **2001**, *101*, 1869–1880. [CrossRef] [PubMed]
45. Ghezzi, C.E.; Rnjak-Kovacina, J.; Kaplan, D.L. Corneal tissue engineering: Recent advances and future perspectives. *Tissue Eng. Part B Rev.* **2015**, *21*, 278–287. [CrossRef] [PubMed]
46. Tegtmeyer, S.; Papantoniou, I.; Müller-Goymann, C.C. Reconstruction of an in vitro cornea and its use for drug permeation studies from different formulations containing pilocarpine hydrochloride. *Eur. J. Pharm. Biopharm.* **2001**, *51*, 119–125. [CrossRef]
47. Reichl, S.; Bednarz, J.; Müller-Goymann, C. Human corneal equivalent as cell culture model for in vitro drug permeation studies. *Br. J. Ophthalmol.* **2004**, *88*, 560–565. [CrossRef] [PubMed]
48. Quantock, A.J.; Winkler, M.; Parfitt, G.J.; Young, R.D.; Brown, D.J.; Boote, C.; Jester, J.V. From nano to macro: Studying the hierarchical structure of the corneal extracellular matrix. *Exp. Eye Res.* **2015**, *133*, 81–99. [CrossRef] [PubMed]
49. Pitre, J.J., Jr.; Kirby, M.A.; Li, D.S.; Shen, T.T.; Wang, R.K.; O'Donnell, M.; Pelivanov, I. Nearly-incompressible transverse isotropy (NITI) of cornea elasticity: Model and experiments with acoustic micro-tapping OCE. *Sci. Rep.* **2020**, *10*, 12983. [CrossRef]
50. Antman-Passig, M.; Shefi, O. Remote magnetic orientation of 3D collagen hydrogels for directed neuronal regeneration. *Nano Lett.* **2016**, *16*, 2567–2573. [CrossRef]
51. Norman, J.J.; Desai, T.A. Control of cellular organization in three dimensions using a microfabricated polydimethylsiloxane–collagen composite tissue scaffold. *Tissue Eng.* **2005**, *11*, 378–386. [CrossRef]
52. Sun, M.G.; Son, T.; Crutison, J.; Guaiquil, V.; Lin, S.; Nammari, L.; Klatt, D.; Yao, X.; Rosenblatt, M.I.; Royston, T.J. Optical coherence elastography for assessing the influence of intraocular pressure on elastic wave dispersion in the cornea. *J. Mech. Behav. Biomed. Mater.* **2022**, *128*, 105100. [CrossRef]